Thermospheric Neutral Density Variation during the "SpaceX" Storm: Implications from Physics-based Whole Geospace Modeling

Dong Lin[1], Wenbin Wang[1], Katherine Garcia-Sage[2], Jia Yue[2,3], Viacheslav Merkin[4], Joseph M. McInerney[1], Kevin Pham[1], and Kareem Sorathia[4]

[1]High Altitude Observatory, National Center for Atmospheric Research, Boulder, CO, USA.
[2]NASA Goddard Space Flight Center, Greenbelt, MD, USA
[3]Catholic University of America, Washington, DC, USA
[4]Applied Physics Laboratory, Johns Hopkins University, Laurel, MD, USA

Key Points:

- Our model predicts up to $\sim 150\%$ enhancement in neutral density along Starlink orbit during a moderate geomagnetic storm on 3-4 February 2022.
- Empirical models tend to underestimate storm effects in thermospheric density enhancement.
- The whole geospace model resolves the gradual recovery and wave perturbations missed by empirical models.

Corresponding author: Dong Lin, ldong@ucar.edu

Abstract

The Starlink satellites launched on 3 February 2022 were lost before they fully arrived in their designated orbits. The loss was attributed to two moderate geomagnetic storms that occurred consecutively on February 3-4. We investigate the thermospheric neutral mass density variation during these storms with the Multiscale Atmosphere-Geospace Environment (MAGE) model, a first-principles, fully coupled geospace model. Simulated neutral density enhancements are validated by Swarm satellite measurements at the altitude of 400-500 km. Comparison with standalone TIEGCM and empirical NRLMSIS 2.0 and DTM-2012 models suggests better performance by MAGE in predicting the maximum density enhancement and resolving the gradual recovery process. Along the Starlink satellite orbit in the middle thermosphere (~ 200 km altitude), MAGE predicts up to 150% density enhancement near the second storm peak while standalone TIEGCM, NRLMSIS 2.0 and DTM-2012 suggest only $\sim$ 50% increase. MAGE also suggests altitudinal, longitudinal, and latitudinal variability of storm-time percentage density enhancement due to height dependent Joule heating deposition per unit mass, thermospheric circulation changes, and travelling atmospheric disturbances. This study demonstrates that a moderate storm can cause substantial density enhancement in the middle thermosphere. Thermospheric mass density strongly depends on the strength, timing, and location of high-latitude energy input, which cannot be fully reproduced with empirical models. A physics-based, fully coupled geospace model that can accurately resolve the high-latitude energy input and its variability is critical to modeling the dynamic response of thermospheric neutral density during storm time.

Plain Language Summary

On February 3, 2022, 40 Starlink satellites were launched by the SpaceX Corporation when a moderate geomagnetic storm occurred, followed by another storm on February 4. The storm activities have been regarded as the culprit for the loss the Starlink satellites afterwards. Although strong geomagnetic storms are well-known to be able to increase the neutral atmospheric mass density so as to satellite drag in the thermosphere where many space vehicles are orbiting around the Earth, a not-so-strong storm was not expected to bring such huge impacts based on engineering design evaluation using empirical atmospheric density models. This study compares the performance of a state-of-the-art physics-based, fully coupled whole geospace model and empirical models in predicting the neutral mass density variation in the thermosphere. It turns out that the physics-based model is more accurate in capturing the magnitude of storm enhancement of neutral density. It also resolves the gradual recovery process even though it is not reflected in some geomagnetic indices that are used to drive the empirical models. Using such a first-principles whole geospace model is suggested as a necessary step in future space weather applications.

1 Introduction

The ionosphere-thermosphere (I/T) system is an important atmospheric region where many space vehicles are orbiting around the Earth. The thermospheric density is a critical parameter in determining the drag on those satellites and the resulting stability of the satellites and their orbits, as well as potential for collision with other objects. The variability of neutral density with geomagnetic conditions such as storms can thus significantly affect satellite operations. It is well-known that the I/T system is driven by internal dynamics and external forcing from the sun (e.g. Richards, 2001; L. Liu et al., 2011), magnetosphere (e.g., Fuller-Rowell et al., 1994; J. Forbes et al., 1996; Wang et al., 2008; Zhu et al., 2022), and lower atmosphere (e.g., H.-L. Liu et al., 2013; H.-L. Liu, 2016). Therefore, thermospheric density exhibits complicated temporal variability across a broad range of time scales, including solar cycle, seasonal, diurnal, and geomagnetic storm-time variations, and spatial variations with latitude, longitude, and altitude (e.g., J. M. Forbes, 2007; Qian & Solomon, 2012).

Geomagnetic storms, especially major ones with Dst minimum less than -100 nT, can greatly disturb the I/T system and thermospheric density (e.g., Fuller-Rowell et al., 1994; J. Forbes et al., 1996). Using measurements from the Satellite Electrostatic Triaxial Accelerometer experiment in the middle thermosphere ($\sim$ 200 km altitude), J. Forbes et al. (1996) found that the thermospheric density increased by 50-70% in the dayside high latitude region when Kp increased from 1-2 to 4-7. Rhoden et al. (2000) also reported an increase of density by 134% from Kp 1 to 6. CHAMP and GRACE data have been widely used in the recent two decades to study the upper thermospheric density variation at 400-500 km altitude in the noon and midnight sectors. H. Liu and Lühr (2005) reported a maximum density enhancement of 400-500% during the 29-31 October 2003 super storm. Bruinsma et al. (2006) found a global density increase of 300-800% during the 20-21 November 2003 storm. Lei et al. (2010) reported a storm time density increase of 200-400% during the main phase of the 7-9 November 2004 major storm.

The storm-time enhancement of thermospheric density is caused by increased magnetospheric energy input at high latitudes. During storm times, high latitude ionospheric plasma convection is enhanced and causes a substantial increase in Joule heating. Joule heating rate is proportional to ionospheric Pedersen conductivity, which usually maximizes in the E region and is increased during storms too, due to enhanced auroral precipitation (Campbell, 2003). Auroral precipitation also brings extra energy inputs to the I/T system in the auroral region through ionization, dissociation, and excitation of neutral constituents (Qian & Solomon, 2012). Therefore, storm effects on thermospheric density are expected to depend on many factors, including geomagnetic activity level and altitude. Furthermore, disturbances at high latitudes are transmitted to lower latitudes by storm-induced changes in large scale circulation and travelling atmospheric disturbances. There is typically a few hours time delay in the thermosphere responses between low and high latitudes (e.g., Bruinsma et al., 2006). Consequently, the storm time variation of thermospheric density becomes a global phenomenon. The dependence of thermospheric and ionospheric responses on three-dimensional spatial distribution of Joule heating rate and ion drag, which is controlled by the characteristics of a particular storm event, such as the onset time, solar wind condition, type, strength and duration of the event, makes it more challenging to accurately characterize storm time variation of thermosphere neutral density.

However, satellite and ground-based measurements can only cover certain local longitude/latitude regions, altitudes and local times during a storm. To provide a global coverage and for prediction purposes, various I/T models have been developed and used to investigate thermospheric density distribution and variability. Empirical models use statistical relations with geomagnetic indices and solar fluxes to derive neutral density as a function of latitude, longitude, altitude and time (e.g. Emmert et al., 2021; Hedin, 1987; Bowman et al., 2008; Bruinsma, 2013). While empirical models such as NRLMSIS 2.0 are good at characterizing the average density distribution and longer term variability, they usually have difficulty in resolving storm-time responses as these models may easily miss the dynamic variability of the storm-time I/T system on small spatial and temporal scales (e.g. Rhoden et al., 2000; Bruinsma et al., 2006). On the other hand, recent developments in whole geospace modeling shows great advances in characterizing storm-time large and mesoscale structures such as traveling atmospheric disturbances (Pham et al., 2022). A physics-based global geospace model solves for I/T state from first-principles equations and treats the I/T as a component of the coupled geospace system.

During the past few years of solar minimum, major geomagnetic storms have become rare. Storm-time thermospheric density variation and its impacts on satellite drag appear to be less concerning. However, a moderate geomagnetic storm that occurred on

3-4 February 2022 was reported to have caused the loss of 40 Starlink satellites of the SpaceX Corporation orbiting in the middle thermosphere. This storm is hereinafter referred to as the "SpaceX storm" (Hapgood et al., 2022). Empirical models such as the NRLMSIS 2.0 and DTM models and standalone ionosphere-thermosphere general circulation models such as TIEGCM predict relatively moderate density enhancement of about 50% at the Starlink orbit altitude of $\sim$ 200 km, which is less likely to be strong enough to account for the satellite drag that failed the satellites (e.g., Dang et al., 2022). In this study, we use a newly developed whole geospace model, the Multiscale Atmosphere-Geospace Environment (MAGE), to investigate the thermospheric density variations during the "SpaceX storm" event. We also compare the performance of MAGE with several other models, including a standalone I/T general circulation model (TIEGCM) (Richmond et al., 1992), the empirical models of NRLMSIS 2.0 (Emmert et al., 2021) and the Drag Temperature Model (DTM) (Bruinsma, 2013).

2 Methodology

The MAGE model is a whole geospace model that is being developed with the aim to explore the magnetosphere-ionosphere-thermosphere as a tightly coupled system. The current version used here, MAGE 1.0, consists of the Grid Agnostic MHD for Extended Research Applications (GAMERA) global magnetohydrodynamic (MHD) model of the magnetosphere (Zhang et al., 2019; Sorathia et al., 2020), the Rice Convection Model (RCM) of the ring current (Toffoletto et al., 2003), Thermosphere Ionosphere Electrodynamics General Circulation Model (TIEGCM) of the upper atmosphere (Richmond et al., 1992), and the RE-developed Magnetosphere-Ionosphere Coupler/Solver (REMIX) (Merkin & Lyon, 2010). MAGE is driven by observed solar wind and interplanetary magnetic field (IMF) at its upstream boundary. Magnetosphere-driven high latitude ionospheric convection and auroral precipitation are used to drive the TIEGCM. Details about the model configuration can be found in Pham et al. (2022) and Lin et al. (2021).

Figure 1 shows the solar wind and IMF conditions and geomagnetic activity indices of Kp and SymH from February 1 to February 6. A coronal mass ejection arrived at the Earth by the end of February 1, manifested by abruptly increased solar wind speed and density and oscillating IMF. IMF B_Z suddenly dropped to -12 nT at 23 UT on February 1 although the southward B_Z lasted for less than an hour. Solar wind speed increased from $\sim$ 350 km/s to nearly 500 km/s. Solar wind density increased from $\sim$ 4/cc to more than 10/cc, resulting in a dynamic pressure enhancement by more than five times. A sudden commencement can be identified from the SymH index. IMF B_Z stayed mostly northward on February 2 except a two-hour interval of -6 nT. The IMF smoothly turned southward on February 3 and reached a minimum of -18 nT at 10 UT. The B_Z turning was accompanied by B_Y rotation from +10 nT to -18 nT. The SymH index showed a typical main phase feature of rapid decrease (Wanliss & Showalter, 2006) and reached a minimum value of -75 nT at $\sim$ 11 UT on February 3. At around 12 UT on February 3, another dynamic pressure impulse arrived at the Earth with northward IMF. The first storm gradually recovered till 4 UT on February 4 when IMF B_Z turned to -10 nT and stayed southward for the next two days. A second storm can be seen in the SymH index with another minimum of -60 nT at 22 UT on February 4. The storm activities were recovering since February 5. In this study, the observed solar wind and IMF conditions (Figures 1a-1c) were used to drive the MAGE model to investigate the thermospheric mass density variation during the storm and its potential impacts on the Starlink satellites which were launched at around 18 UT on February 3 (vertical red dashed line).

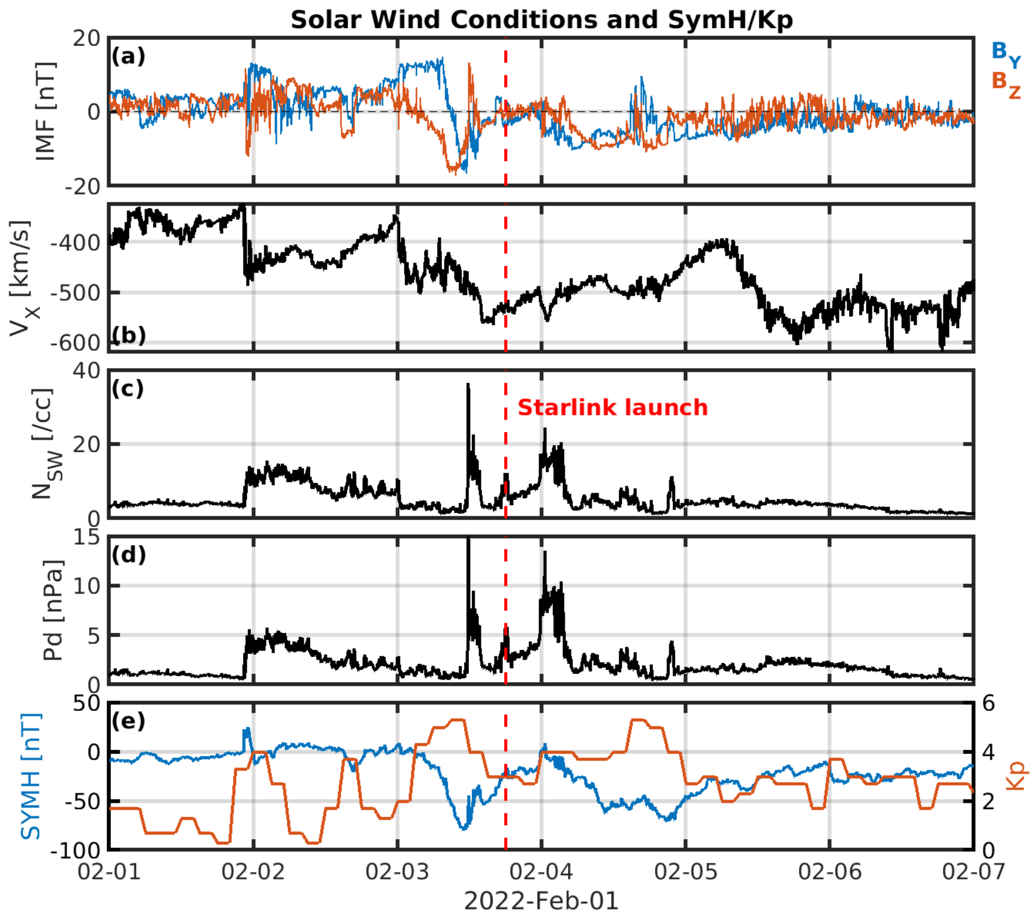

Figure 1. Solar wind/IMF data and SymH/Kp indices during 1-6 February 2022. (a) IMF B_Y (blue) and B_Z (red) in the Solar Magnetic (SM) coordinates. (b) Solar wind velocity V_X. (c) Solar wind density N_{SW}. (d) Solar wind dynamic pressure P_d. (e) SymH (blue) and Kp indices (red). The vertical red dashed line indicates the launch time of Starlink satellites.

3 Results and Discussion

3.1 Neutral density variations at Swarm orbit altitude

We start by analyzing the neutral density variations measured by the Swarm satellites during the SpaceX storm event. This is because the neutral densities derived from the Starlink orbit are not yet publicly available, and when available, will require calibration and comparison against science grade neutral density data. The Swarm satellites A and B provide such science grade neutral densities (van den IJssel et al., 2020). Although the Swarm satellite orbits are higher than the newly-launched Starlink satellites during this time, the densities along the Swarm orbit demonstrate the response of the thermosphere to the storm and provide a baseline to assess the accuracy of the model responses.

Figures 2a-2b show the relative variation of the neutral density $\Delta\rho/\rho_0$ observed by the Swarm A and B satellites. Here ρ_0 is the daily mean density on February 1, the quiet-day reference before the storm. $\Delta\rho = \rho - \rho_0$ is the absolute variation of neutral density from ρ_0. The relative variation is averaged over each orbit period, i.e., 93 min for

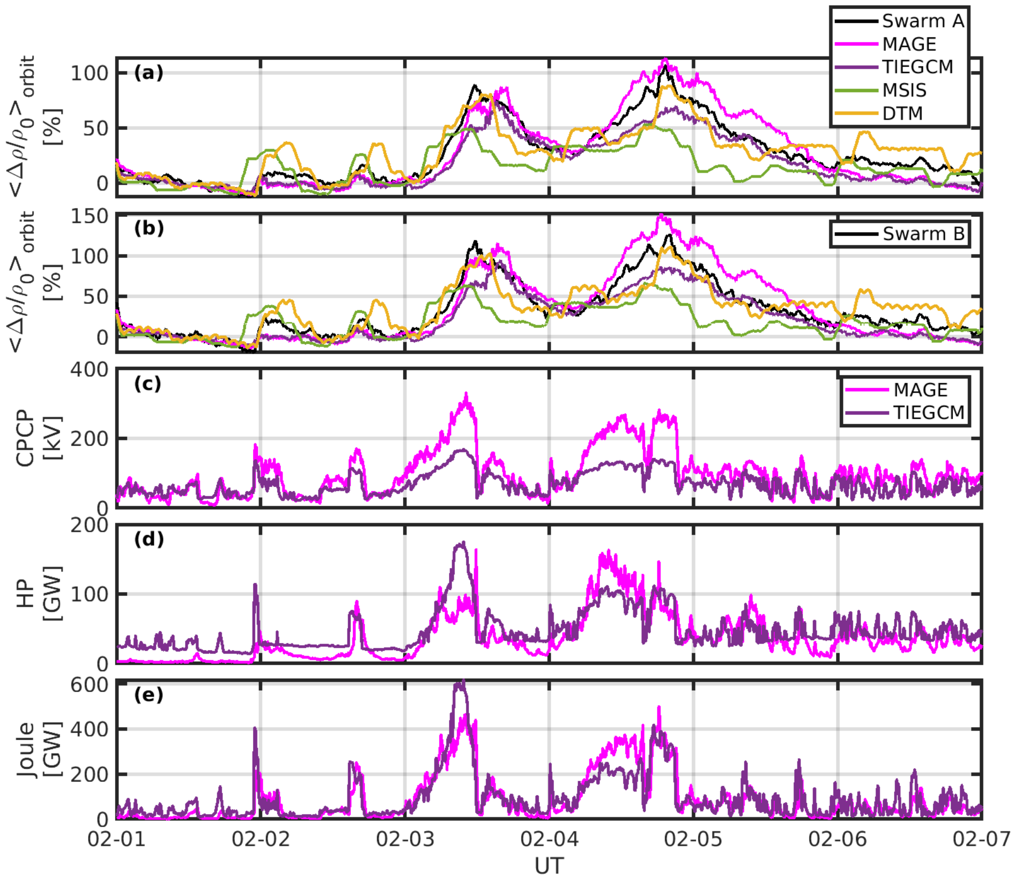

Figure 2. (a-b) Neutral density variations measured by the Swarm satellite (black) and simulated by the MAGE (magenta), standalone TIEGCM driven by the Weimer empirical convection model (purple), NRLMSIS 2.0 (green), and DTM-2012 (yellow) models during the SpaceX storm event. The density variation is normalized by the daily mean value on February 1 and averaged over each orbit. (c-e) Cross-polar cap potential (CPCP), hemisphere power (HP), and integrated high latitude Joule heating rate in the northern hemisphere simulated by the MAGE and standalone TIEGCM.

Swarm A and 95 min for Swarm B. Swarm C results are not shown because they are identical to those from Swarm A, which shared the same orbit. Swarm A and B has an average orbit altitude of 440 km and 515 km, respectively.

As shown in Figure 2a, Swarm A observed an increase of neutral density starting on February 3, normalized by the daily mean density of February 1. It reached 87% around 12 UT when the first storm reached the SymH minimum. During the recovery phase of the first storm, the orbit mean density decreased, but it still maintained a perturbation level that was $\sim$ 25% higher than the quiet day reference value by 4 UT on February 4. After the second storm started, the mean density at Swarm A orbit increased again to a peak value of 105% at around 20 UT on February 4. The Swarm A-measured density then gradually decreased to the pre-storm level during the second recovery phase by February 7. The density variation observed by Swarm B showed a similar two peak pattern to Swarm A observations. The peak values of the relative increase are 118% and

124% during the two storms, slightly higher than the values observed by Swarm A as Swarm B orbit is higher.

MAGE-simulated neutral density variations are shown by the magenta curves in Figures 2a and 2b. The neutral density is sampled along the Swarm trajectories in MAGE outputs, which are saved every 5 minutes. The density variation is also normalized by the daily mean density of February 1 and averaged over each orbit. It can be seen that the MAGE model reproduces the relative density variation in quantitative agreement with Swarm satellite observations. The magnitude of the MAGE-simulated relative density changes and the temporal variations in the first storm period are close to Swarm observation except at $\sim$ 16 UT on February 3 when MAGE predicts a perturbation peak which is not seen in the data. For the second storm, the MAGE results appear to overestimate the perturbations around the storm peak at $\sim$ 18 UT as well as in the storm recovery phase on February 5. Nevertheless, the observed major density enhancements of $\sim$ 100% are captured by the MAGE model during both storm peaks on February 3 and February 4. MAGE also reproduces the process of gradual increase and recovery during different phases of the two storms.

As a comparison, the relative neutral density variations simulated by the standalone TIEGCM, and empirical NRLMSIS 2.0 and DTM-2012 models are shown with the purple, green, and yellow curves in Figures 2a and 2b. The standalone TIEGCM simulation is driven by the Weimer (2005) convection model with the same solar wind/IMF conditions for MAGE run. The NRLMSIS 2.0 model is driven by the 3-hourly Ap index, and daily and 81-day average F10.7 indices. The DTM-2012 model is driven by hourly Hpo (Yamazaki et al., 2022) and solar F30 indices. It can be seen that the Weimer-driven TIEGCM simulation underestimated the relative density enhancement during both storms (purple curves). In particular, the second storm peak on February 4 was only $\sim$ 65% higher than the quiet-day reference along the Swarm A orbit while the Swarm A data and MAGE simulation both suggest a $\sim$ 110% enhancement. DTM-2012 (yellow curves) predicted comparable density enhancements during the two storms but overestimated the density enhancement on February 2 and February 6 when the geomagnetic activity level was relatively low. The model also underestimated density perturbations in the recovery phase of the first storm and the initial phase of the second storm. NRLMSIS 2.0 (green curves) underestimated the density enhancement for both storms. Its peak value is about half of that measured by Swarm. The density enhancement simulated by NRLMSIS 2.0 also occurred earlier than Swarm measurements, probably due to the timing uncertainty of the 3-hour Ap index that was used to drive the model.

Figures 2c-2e show the strength of high latitude convection pattern and energy inputs simulated by the MAGE model and standalone TIEGCM. The convection strength is indicated by the cross-polar cap potential (CPCP). The hemisphere power (HP) is the total precipitation energy flux integrated over each hemisphere above 45° magnetic latitude. This latitude range is chosen to cover the large-scale convection driven by the magnetospheric dynamics during the storms. During the first storm, the density enhancement was accompanied by greatly enhanced CPCP, HP, and total Joule heating rate. CPCP reached $\sim$ 300 kV, HP exceeded 100 GW and Joule heating rate was more than 400 GW at 12 UT on February 3 in both hemispheres. Although CPCP, HP, and Joule heating all dropped suddenly after the first storm peak at $\sim$ 12 UT due to northward turning of IMF (Figure 1a), the neutral density remained enhanced and recovered with a much slower rate. The gradual recovery of neutral density is more evident after the second storm on February 4. Both the Swarm observed and MAGE simulated neutral density did not recover to the pre-storm level until February 6 even though the Kp index dropped to below 3 on February 5 (Figure 1e) and drove a fast recovery of the MSIS neutral density.

Figure 2c also shows that the TIEGCM CPCP, which is essentially the Weimer (2005) model, is only 50% of the MAGE CPCP. Compared to the CPCP, the HP and total Joule heating rate in the Weimer driven TIEGCM are closer to MAGE results and sometimes higher (Figures 2d-2e). Note the CPCP, HP, and Joule are all hemisphere integrated quantities. Their spatial distribution and temporal evolution of these quantities also play a critical role in the storm time variation of the ionosphere-thermosphere system. Pham et al. (2022) found that MAGE simulated neutral density has a better agreement with CHAMP and GRACE measurements compared to Weimer driven standalone TIEGCM, even though the MAGE run has a lower Joule.

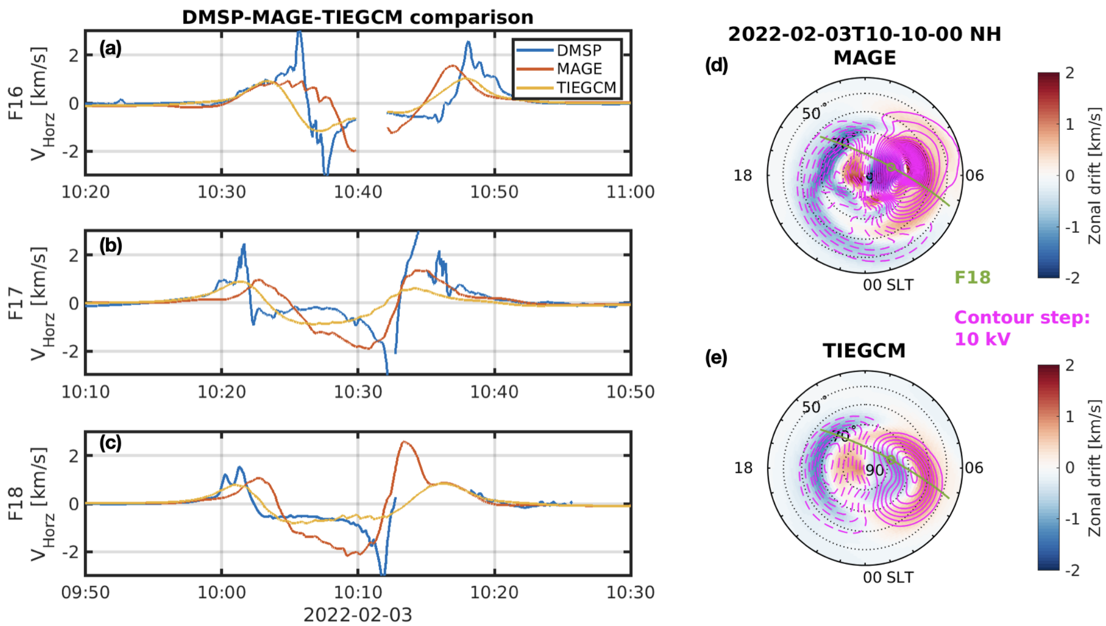

Figure 3. (a-c) Cross-track ion drift velocity measured by DMSP and sampled from MAGE and standalone TIEGCM simulation results. (d-e) Zonal ion drift and convection potential contour simulated by MAGE and standalone TIEGCM.

The MAGE simulated high latitude convection is further validated with DMSP measurements of cross track ion drift. Figure 3 shows the comparison of V_{Horz} measured by DMSP (blue), and simulated by MAGE (red) and standalone TIEGCM (yellow) at around 10:10 UT on February 3, when the CPCP reached the maximum value. The ion drifts are smoothed with a moving average over 15s to remove the observed oscillations on a spatial scale smaller than the grid size, which is 1.25° in both MAGE and standalone TIEGCM. The V_{Horz} comparison shows that the TIEGCM convection is generally weaker than DMSP measurements, while MAGE simulation results are more consistent with DMSP data. Note CPCP cannot be directly measured without a global coverage of the entire convection pattern. DMSP V_{Horz} can only partially represent CPCP when the trajectory is close to the convection cell centers, which is roughly the case for DMSP F18 during the interval around 10:10 UT (see the green curve and magenta contours in Figures 3d-3e). Figures 3d-3e show the zonal ion drift and convection potential contour at 2022-02-03/10:10 UT. The convection contour is equally spaced by every 10 kV. While the TIEGCM sampling of V_{Horz} agrees well with DMSP F18 data in the polar cap, its dawnside side convection velocity is much weaker than DMSP measurements after 10:10 UT, suggesting the CPCP from Weimer is indeed underestimated. The MAGE sampling of V_{Horz} resolves the dawnside convection with a much better agreement, including resolving the $\sim$ 2 km/s convection flow, although the MAGE results appear to be overestimated in the polar cap. A similar comparison is found for DMSP F16 and F17.

In this study, we focus on the large scale storm time variation of thermospheric neutral density, which is more relevant to the accumulated effects on satellite drag. Hence, we present the orbit averaged relative variations. The absolute values of neutral density in the model are sometimes higher than Swarm and GRACE Follow-on (FO) measurements, which is not shown here. The difference in absolute values is related to the initial state of TIEGCM used by MAGE, which shows higher density than Swarm and GRACE-FO data. However, with the initial offset removed, the relative variation in MAGE simulation results does show a quantitative agreement with observations in terms of the storm time neutral density evolution.

3.2 Neutral density variations along the Starlink orbit

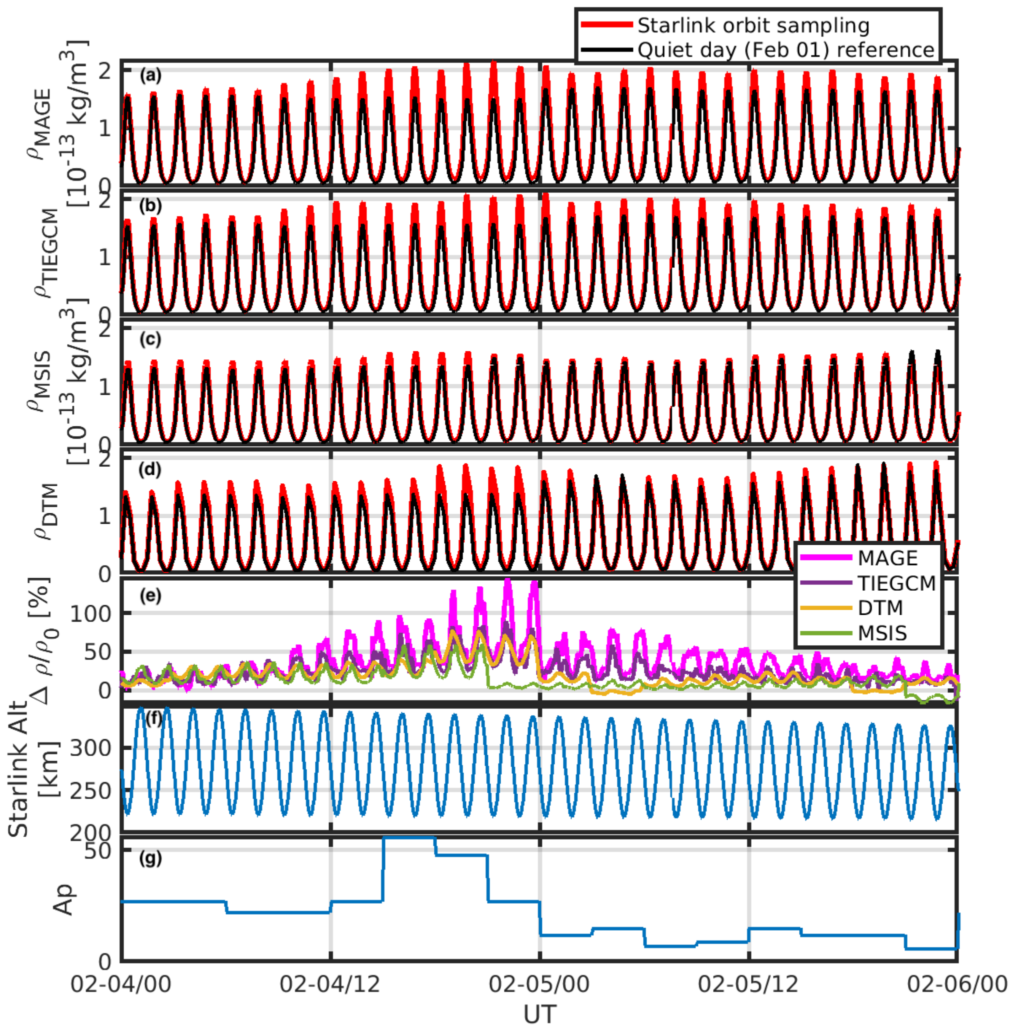

Figure 4. Neutral density variations along the Starlink orbit calculated by (a) MAGE, (b) TIEGCM, (c) DTM-2012, and (d) NRLMSIS 2.0. (e) Relative variations of neutral density based on the values on February 1 at the same UT and location. (f) Starlink altitude. (g) The Ap index used to drive NRLMSIS 2.0.

We now turn to an analysis of the modeled neutral density variation along the Starlink orbit. Since Starlink was not in orbit before February 4, we compare the February

4 and 5 density with that on February 1 at the same orbital location to investigate the storm effects. The Starlink orbit data was derived from publicly available NORAD Two-Line Elements (TLEs) obtained from CelesTrak (https://celestrak.org/). The altitude of the Starlink orbit ranged from 200 km to 330 km (Figure 4f), involving a density difference of more than one order of magnitude. Therefore, we do not use orbit average but use a point-to-point comparison of neutral density. Figures 4a-4d show the neutral density simulated by MAGE, standalone TIEGCM, DTM-2012, and NRLMSIS 2.0, respectively. The red curves show the density sampled along the Starlink orbit and the black curves show the density sampled at the same location and UT on February 1.

By comparing the red and black curves, all four models show storm time enhancement of neutral density along the Starlink orbit after it was launched. However, different models predict vastly different levels of relative density enhancement. To better illustrate the storm effects, we compare the ratio of neutral density to February 1 for MAGE, TIEGCM, DTM-2012 and NRLMSIS 2.0 in Figure 4e. Despite a periodic variation that is closely related to the orbit altitude, the MAGE results suggest a density enhancement by up to 150% during the second storm on February 4 (magenta curve). The orbital maximum enhancement dropped to $\sim 75\%$ after 0 UT on February 5 and slowly recovered to $\sim 20\%$ by the end of February 6. The variation of neutral density in MAGE simulation results is determined by the high latitude energy input, which is shown in Figures 2c-2f. The hemisphere power and integrated Joule heating were greatly enhanced during the two storms, which increase the neutral temperature and elevate the atmosphere, as well as the neutral density along the satellite orbit. In the storm recovery phase when IMF B_Z turned northward, high-latitude energy inputs significantly decreased and the I/T system began to recover to its undisturbed state before the storms. This recovery process is slow (Burns et al., 1991) and the density enhancement simulated by MAGE also takes time to dissipate as shown in Figure 4, as well as for the Swarm densities at higher altitudes (Figures 2a and 2b).

On the other hand, standalone TIEGCM (purple), DTM-2012 (yellow) and NRLMSIS 2.0 (green) results only suggest an enhancement of at most $50-75\%$ during the second storm on February 4. Particularly, the NRLMSIS 2.0 simulated neutral density enhancement dropped to near zero immediately at 21 UT on February 4. The variation of NRLMSIS 2.0 results can be largely attributed to the 3-hour Ap index that is used as the input for the model. Note the F10.7 index inputs for all models are daily values and only varied by less than 5% during these events (between 120 and 126). Figure 4g shows that the Ap index increased from 27 to 56 at 15 UT and decreased from 48 to 27 at 21 UT, which yields a moderate density enhancement in NRLMSIS 2.0 results (Figure 4c). DTM-2012 and standalone TIEGCM results show a rapid recovery on February 5, in contrast to the gradual recovery shown in MAGE results. While the Ap index does suggest a rapid recovery of geomagnetic activity at auroral latitudes on February 5, the SymH index (Figure 1e) and Swarm measurements of mass density (Figures 4a-4b) reveal that the storm effects were still present on February 5 and it took a longer time for the thermospheric neutral density to recover. This contrast also highlights the need to properly represent the recovery phase in order to accurately predict the mass density variation during the entire process of geomagnetic storms.

3.3 Neutral density variation with altitude

The density ratios along the Starlink orbit exhibit a periodic pattern, which is mainly attributed to the altitudinal variation of the orbit. In fact, comparison of the results at Swarm A, Swarm B, and Starlink orbits also suggests an altitudinal dependence of storm time neutral density variations. To better understand the altitudinal dependence, we compared the vertical distributions of density enhancement in Figure 5 with MAGE simulation results. The density variation relative to the same location and UT on February 1 is evaluated for all longitudes and latitudes. The average variation over all longitudes

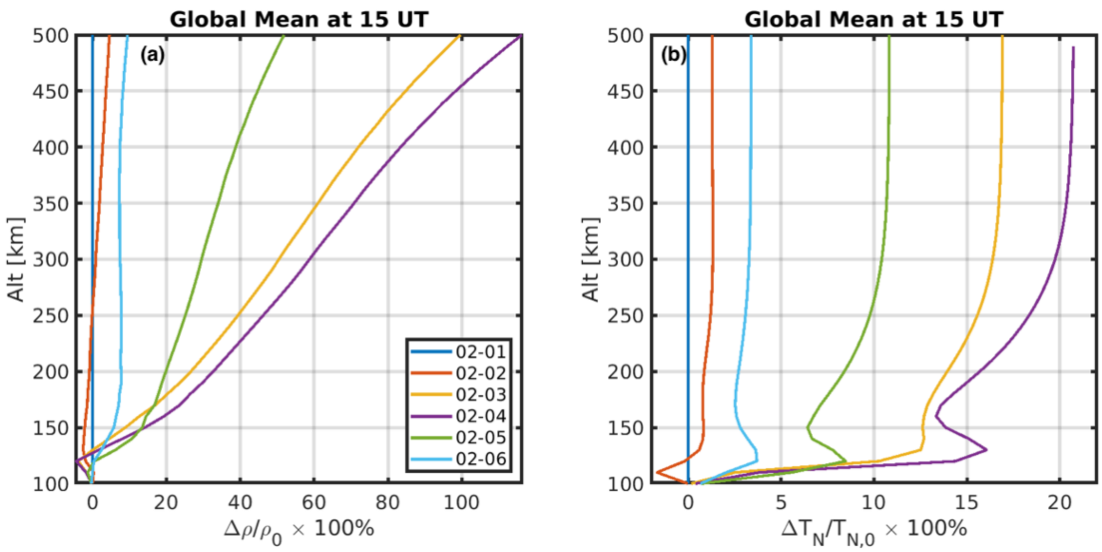

Figure 5. Global mean relative neutral density (a) and neutral temperature (b) variations with altitude at 15 UT on different days.

and latitudes is shown in Figure 5a for 15 UT of six consecutive days from February 1 to 6. From February 3 to February 5 (yellow, purple, and green), the percentage density enhancement increases nearly linearly with altitude. In the altitude range between 200 km and 330 km where Starlink orbit is located, global thermospheric neutral density is on average enhanced by 40−60% at 15 UT on February 4 and by 20-30% on February 5.

Figure 5b shows a similar analysis for neutral temperature variation. Compared to the quasi-linear dependence of density enhancement on altitude during the storm time, the neutral temperature enhancement is nearly constant above 200-300 km altitude. During the first storm on February 3, the neutral temperature was globally enhanced by 10%-17% below 300 km altitude and uniformly enhanced by 17% above 300 km. The temperature enhancement was more than 20% at high altitudes near the peak of the second storm at 15 UT on February 4.

There is a local peak of neutral temperature enhancement at $\sim$ 125 km altitude during the storm time. The temperature enhancement peak is attributed to the altitudinal distribution of Pedersen conductivity, which has a maximum value around this height and results in the maximum Joule heating deposition (Campbell, 2003). The storm time temperature enhancement increases with altitude because the background density decreases exponentially while Joule heating rate per unit mass increases with altitude (Huang et al., 2012; Deng et al., 2011).

In Figure 5 we only show the comparison below 500 km altitude to ensure the altitudinal range is covered by MAGE at all longitudes and latitudes for all six days. Note in MAGE, the TIEGCM grid is defined by pressure levels which vary with altitude/temperature depending on many factors including solar zenith angle, solar radiation and magnetospheric conditions. We show 15 UT of each day because it is near the peak of both two storms. Other UTs also show similar dependencies on altitude. The density enhancement is contributed mostly by the increased thermospheric temperature and thus a larger atmospheric scale height, which raises the altitudes of the pressure surfaces. Thermospheric composition also contributes to neutral density changes (Lei et al., 2010). Consequently, in the altitude coordinates in which satellite observations are made the neutral density at the same altitudes during the storms is increased.

3.4 Neutral density variation with latitude

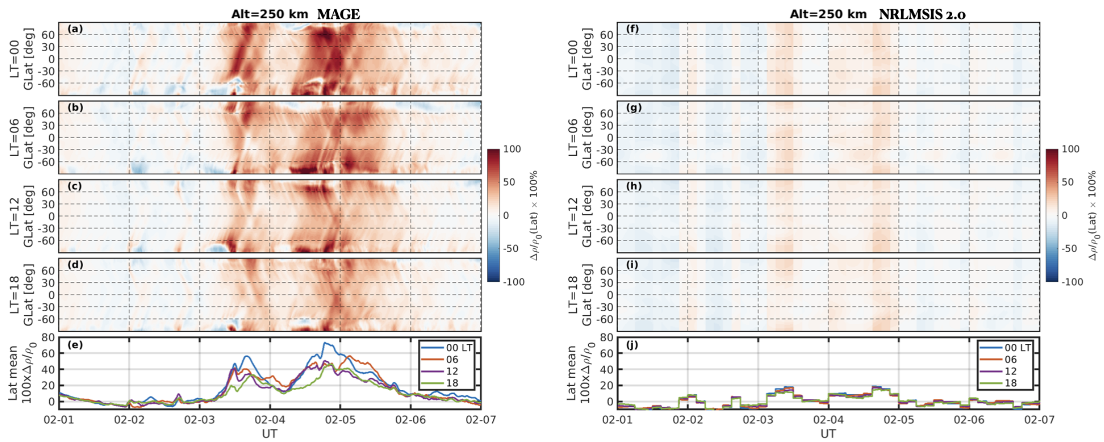

Figure 6. MAGE (left) and NRLMSIS 2.0 (right) simulated neutral density variations at different latitudes and four local times at the altitude of 250 km.

While Figure 5a suggests that the global mean density enhancement is up to 40% and temperature enhancement is up to 18% during the storms at the average Starlink orbit altitude of 250 km, thermospheric response exhibits substantial spatial and temporal variability. Figure 6 shows the latitudinal and UT dependence of neutral density variation simulated by MAGE and NRLMSIS 2.0 at four different local times (LTs): midnight (00LT), dawn (06LT), dusk (18LT), and noon (12LT). The relative density variation is normalized by the daily mean density at the same latitude and local time on February 1.

Latitudinally, the relative density variation is generally stronger at high latitudes than at middle and low latitudes. For instance, at 15 UT on February 4 along 00 LT, the relative density enhancement is $\sim 80\%$ at $60°$ geographical latitude and $\sim 50\%$ at $-85°$ geographical latitude, whereas it is less than 40% within $20°$ from the equator. The stronger enhancement at higher latitudes is attributed to the storm time high latitude energy inputs from the magnetosphere, which are mostly deposited in the auroral zone and polar cap regions. As shown in Figure 2c, the CPCP is greatly enhanced during the two storms, indicating a much stronger high latitude convection. On the other hand, the magnetospheric precipitation is also intensified during storm time as represented by the hemispheric power (Figure 2d). High-latitude energy inputs are localized and vary with time (Pham et al., 2022). Therefore, storm-time neutral density changes depend on local time. For instance, the latitudinal mean density changes peak at different UTs for different LTs (Figure 6e). On February 3, the density changes attain the first peak almost at the same UTs for all LTs, whereas for the second peak on the same day occurred first at midnight, followed by peaks at dusk, noon and dawn. Similar LT dependence is also seen during the second storm on February 4. In addition, the midnight sector has the largest relative density perturbations while noon experiences the least changes for both storms.

The right column shows that same latitudinal variations of neutral density from the NRLMSIS 2.0 model. Neutral density perturbations are noticeably smaller than those simulated by the MAGE model, as summarized by the latitudinal mean variations shown in Figure 6e for MAGE and Figure 6j for NRLMSIS 2.0. The NRLMSIS 2.0 results do not show obvious LT dependence either. It also does not have the propagation character of density perturbations as seen in MAGE results, that is, there is an obvious time delay between the high latitude and low latitude density variations. This is understandable as NRLMSIS 2.0 is an empirical model and it does not include dynamics as the first principles model MAGE does.

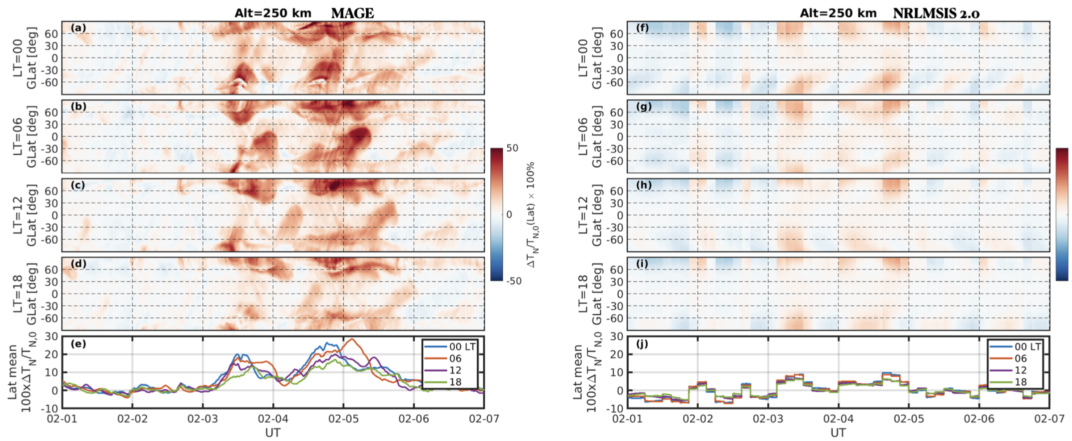

Figure 7. MAGE (left) and NRLMSIS 2.0 (right) simulated neutral temperature variation at different latitudes and four local times at the altitude of 250 km.

In addition to density variations, we also analyzed the responses of neutral temperature during this event. Figures 7a-7d show the keograms of neutral temperature sampled at the same altitude and four local times as in Figure 6. The neutral temperature response shows similar latitudinal and local time dependence, i.e., stronger enhancement at high latitudes than low latitudes during the storms and the nightside undergoes a larger relative neutral temperature variation. However, the temperature variation does not fully resemble that of the neutral density, implying other processes such as composition changes may have contributed to the density variations (e.g., Bruinsma et al., 2006).

The MAGE keograms of density (Figure 6) and temperature (Figure 7) variation also show a time delay of the density and temperature enhancement at different latitudes, which is known to result from traveling atmospheric disturbance (TAD) launched by the increased energy inputs at high latitudes (e.g., Fuller-Rowell et al., 1994; Pham et al., 2022). The comparison between Figures 6(a-e) and Figures 6(f-i) illustrates the contrast between a physics-based whole geospace model and an empirical I/T model. The MAGE model shows clear propagation effects from high to low latitudes which is caused by TADs, whereas the NRLMSIS 2.0 model results hardly show such wave or propagation effects. Again, as mentioned earlier, the first-principles MAGE model solves the dynamics of the I/T system and can resolve large and mesoscale structures like TADs. In addition, as a fully coupled geospace model, MAGE provides a more accurate physical specification of the magnetospheric forcing on the I/T system, including the location and temporal variation of high-latitude energy inputs which is critical to accurately simulate the I/T responses such as TADs to storms (Pham et al., 2022).

The comparison among four local times, midnight, dawn, noon, and dusk, in Figures 6a-6d reveals that neutral density and temperature variations are nonuniform at different local times. Figure 6e shows the latitudinal average of the relative density variations for the four local times. MAGE simulation results indicate that the nightside thermosphere undergoes the largest relative variation in neutral density while the dayside shows the least relative variation across all latitudes on average. The day/night asymmetry is consistent with the observational analysis by J. Forbes et al. (1996) and has to do with the stronger wind surge on the nightside. Increased Joule heating during the storm time forces a global wind surge which undergoes less dissipation by ion drag at low and middle latitudes on the nightside than on the dayside (e.g., J. Forbes et al., 1996). Furthermore, the poleward pressure gradient produced by solar heating works against the equatorward propagation of wind and temperature perturbations during the daytime (Wang et al., 2008).

4 Summary

In this study, we used the MAGE model, a fully coupled whole geospace model, to investigate the neutral density variation during the "SpaceX storm" that occurred on 3-4 February 2022. MAGE-simulated storm-time density enhancements are in quantitative agreement with Swarm satellite measurements in the upper thermosphere. Comparison with the standalone TIEGCM and empirical models such as DTM-2012 and NRLMSIS 2.0 shows an overall better agreement of the physics-based model in simulating neutral density perturbations during the storm event. The MAGE model also resolves the recovery phase as a gradual process rather than an instant change suggested by empirical models driven with the 3-hour Ap index. The better performance of MAGE simulation results is attributed to its capability to dynamically characterize the high-latitude energy inputs as a result of magnetospheric forcing.

We further evaluated the density enhancement along the Starlink satellite orbit in the middle thermosphere near 250 km, where the dynamics are rich but least understood, and observational data are sparse. Despite a moderate storm with a SymH minimum of only -75 nT, the storm time density enhancement simulated by MAGE is up to 150% along the Starlink orbit during the second storm on February 4, much stronger than standalone TIEGCM and empirical model results. The greatly enhanced neutral density is more likely to have caused strong satellite drag that finally failed the Starlink satellites. As we are entering the ascending phase of the current solar cycle, the geomagnetic activity level is expected to increase within the next decade. Reliable observational and numerical capabilities, including those enabled by the fully coupled geospace models like MAGE, to characterize and resolve storm effects on neutral density at all altitudes from middle to upper thermosphere, as well as on other critical I/T parameters, are becoming increasingly important in space weather applications.

Acknowledgments

Dong Lin is thankful to Dr. Liying Qian for an internal review. This work is supported by NASA GCR grant 80NSSC17K0013, DRIVE Science Center for Geospace Storms (CGS) under grant 80NSSC20K0601, HSR grant 80NSSC21K1677, LWS grants 80NSSC20K0356, 80NSSC19K0080, 80NSSC17K0679, 80NSSC21K0008, and 80NSSC20K0199, and NSF CEDAR grant 2033843. This material is based upon work supported by the National Center for Atmospheric Research (NCAR), which is a major facility sponsored by the National Science Foundation under Cooperative Agreement No. 1852977. Computing resources were provided by the High Altitude Observatory at NCAR's Computational and Information Systems Laboratory (CISL).

Data Availability Statement

The OMNI data are available at `https://cdaweb.gsfc.nasa.gov/index.html/`. The Swarm neutral density data is obtained from `http://thermosphere.tudelft.nl`. The simulation data supporting the analysis of this study is archived at this repository: `https://doi.org/10.5065/axkv-me49`.

References

Bowman, B., Tobiska, W. K., Marcos, F., Huang, C., Lin, C., & Burke, W. (2008). A new empirical thermospheric density model jb2008 using new solar and geomagnetic indices. In *Aiaa/aas astrodynamics specialist conference and exhibit* (p. 6438). doi: 10.2514/6.2008-6438

Bruinsma, S. (2013). The semi-empirical thermosphere model dtm2012. In *6th european conference on space debris* (Vol. 723, p. 39).

Bruinsma, S., Forbes, J. M., Nerem, R. S., & Zhang, X. (2006). Thermosphere density response to the 20–21 november 2003 solar and geomagnetic storm from champ and grace accelerometer data. *Journal of Geophysical Research: Space Physics*, *111*(A6). doi: 10.1029/2005JA011284

Burns, A., Killeen, T., & Roble, R. (1991). A theoretical study of thermospheric composition perturbations during an impulsive geomagnetic storm. *Journal of Geophysical Research: Space Physics*, *96*(A8), 14153–14167. doi: 10.1029/91JA00678

Campbell, W. H. (2003). *Introduction to geomagnetic fields*. Cambridge University Press.

Dang, T., Li, X., Luo, B., Li, R., Zhang, B., Pham, K., ... Wang, Y. (2022). Unveiling the space weather during the starlink satellites destruction event on 4 february 2022. *Space Weather*, *20*(8), e2022SW003152. doi: 10.1029/2022SW003152

Deng, Y., Fuller-Rowell, T. J., Akmaev, R. A., & Ridley, A. J. (2011). Impact of the altitudinal joule heating distribution on the thermosphere. *Journal of Geophysical Research: Space Physics*, *116*(A5). doi: 10.1029/2010JA016019

Emmert, J. T., Drob, D. P., Picone, J. M., Siskind, D. E., Jones Jr, M., Mlynczak, M., ... others (2021). Nrlmsis 2.0: A whole-atmosphere empirical model of temperature and neutral species densities. *Earth and Space Science*, *8*(3), e2020EA001321. doi: 10.1029/2020EA001321

Forbes, J., Gonzalez, R., Marcos, F., Revelle, D., & Parish, H. (1996). Magnetic storm response of lower thermosphere density. *Journal of Geophysical Research: Space Physics*, *101*(A2), 2313–2319. doi: 10.1029/95JA02721

Forbes, J. M. (2007). Dynamics of the thermosphere. *Journal of the Meteorological Society of Japan. Ser. II*, *85*, 193–213. doi: 10.2151/jmsj.85B.193

Fuller-Rowell, T., Codrescu, M., Moffett, R., & Quegan, S. (1994). Response of the thermosphere and ionosphere to geomagnetic storms. *Journal of Geophysical Research: Space Physics*, *99*(A3), 3893–3914. doi: 10.1029/93JA02015

Hapgood, M., Liu, H., & Lugaz, N. (2022). *Spacex—sailing close to the space weather?* (Vol. 20) (No. 3). Wiley Online Library. doi: 10.1029/2022SW003074

Hedin, A. E. (1987). Msis-86 thermospheric model. *Journal of Geophysical Research: Space Physics*, *92*(A5), 4649–4662. doi: 10.1029/JA092iA05p04649

Huang, Y., Richmond, A. D., Deng, Y., & Roble, R. (2012). Height distribution of joule heating and its influence on the thermosphere. *Journal of Geophysical Research: Space Physics*, *117*(A8). doi: 10.1029/2012JA017885

Lei, J., Thayer, J. P., Burns, A. G., Lu, G., & Deng, Y. (2010). Wind and temperature effects on thermosphere mass density response to the november 2004 geomagnetic storm. *Journal of Geophysical Research: Space Physics*, *115*(A5). doi: 10.1029/2009JA014754

Lin, D., Sorathia, K., Wang, W., Merkin, V., Bao, S., Pham, K., ... others (2021). The role of diffuse electron precipitation in the formation of subauroral polarization streams. *Journal of Geophysical Research: Space Physics*, *126*(12), e2021JA029792. doi: 10.1029/2021JA029792

Liu, H., & Lühr, H. (2005). Strong disturbance of the upper thermospheric density due to magnetic storms: Champ observations. *Journal of Geophysical Research: Space Physics*, *110*(A9). doi: 10.1029/2004JA010908

Liu, H.-L. (2016). Variability and predictability of the space environment as related to lower atmosphere forcing. *Space Weather*, *14*(9), 634–658. doi: 10.1002/2016SW001450

Liu, H.-L., Yudin, V., & Roble, R. (2013). Day-to-day ionospheric variability due to lower atmosphere perturbations. *Geophysical Research Letters*, *40*(4), 665–670. doi: 10.1002/grl.50125

Liu, L., Wan, W., Chen, Y., & Le, H. (2011). Solar activity effects of the ionosphere: A brief review. *Chinese Science Bulletin*, *56*(12), 1202–1211. doi: 10.1007/s11434-010-4226-9

Merkin, V., & Lyon, J. (2010). Effects of the low-latitude ionospheric boundary condition on the global magnetosphere. *Journal of Geophysical Research: Space Physics*, *115*(A10). doi: 10.1029/2010JA015461

Pham, K., Zhang, B., Sorathia, K., Dang, T., Wang, W., Merkin, V., ... others (2022). Thermospheric density perturbations produced by traveling atmospheric disturbances during august 2005 storm. *Journal of Geophysical Research: Space Physics*, *127*(2), e2021JA030071. doi: 10.1029/2021JA030071

Qian, L., & Solomon, S. C. (2012). Thermospheric density: An overview of temporal and spatial variations. *Space science reviews*, *168*(1), 147–173. doi: 10.1007/s11214-011-9810-z

Rhoden, E., Forbes, J., & Marcos, F. (2000). The influence of geomagnetic and solar variabilities on lower thermosphere density. *Journal of atmospheric and solar-terrestrial physics*, *62*(11), 999–1013. doi: 10.1016/S1364-6826(00)00066-3

Richards, P. (2001). Seasonal and solar cycle variations of the ionospheric peak electron density: Comparison of measurement and models. *Journal of Geophysical Research: Space Physics*, *106*(A7), 12803–12819. doi: 10.1029/2000JA000365

Richmond, A., Ridley, E., & Roble, R. (1992). A thermosphere/ionosphere general circulation model with coupled electrodynamics. *Geophysical Research Letters*, *19*(6), 601–604. doi: 10.1029/92GL00401

Sorathia, K., Merkin, V., Panov, E., Zhang, B., Lyon, J., Garretson, J., ... Wiltberger, M. (2020). Ballooning-interchange instability in the near-earth plasma sheet and auroral beads: Global magnetospheric modeling at the limit of the mhd approximation. *Geophysical research letters*, *47*(14), e2020GL088227. doi: 10.1029/2020GL088227

Toffoletto, F., Sazykin, S., Spiro, R., & Wolf, R. (2003). Inner magnetospheric modeling with the rice convection model. *Space Science Reviews*, *107*(1-2), 175–196. doi: 10.1023/A:1025532008047

van den IJssel, J., Doornbos, E., Iorfida, E., March, G., Siemes, C., & Montenbruck, O. (2020). Thermosphere densities derived from swarm gps observations. *Advances in Space Research*, *65*(7), 1758–1771. doi: 10.1016/j.asr.2020.01.004

Wang, W., Burns, A., Wiltberger, M., Solomon, S., & Killeen, T. (2008). Altitude variations of the horizontal thermospheric winds during geomagnetic storms. *Journal of Geophysical Research: Space Physics*, *113*(A2). doi: 10.1029/2007JA012374

Wanliss, J. A., & Showalter, K. M. (2006). High-resolution global storm index: Dst versus sym-h. *Journal of Geophysical Research: Space Physics*, *111*(A2). doi: 10.1029/2005JA011034

Weimer, D. (2005). Improved ionospheric electrodynamic models and application to calculating joule heating rates. *Journal of Geophysical Research: Space Physics*, *110*(A5). doi: 10.1029/2004JA010884

Yamazaki, Y., Matzka, J., Stolle, C., Kervalishvili, G., Rauberg, J., Bronkalla, O., ... Jackson, D. (2022). Geomagnetic activity index hpo. *Geophysical Research Letters*, e2022GL098860. doi: 10.1029/2022GL098860

Zhang, B., Sorathia, K. A., Lyon, J. G., Merkin, V. G., Garretson, J. S., & Wiltberger, M. (2019). Gamera: A three-dimensional finite-volume mhd solver for non-orthogonal curvilinear geometries. *The Astrophysical Journal Supplement*

Series, *244*(1), 20. doi: 10.3847/1538-4365/ab3a4c

Zhu, Q., Deng, Y., Sheng, C., Anderson, P., & Bukowski, A. (2022). Impact of soft electron precipitation on the thermospheric neutral mass density during geomagnetic storms: Gitm simulations. *Geophysical Research Letters*, *49*(11), e2021GL097260. doi: 10.1029/2021GL097260

Figure1.

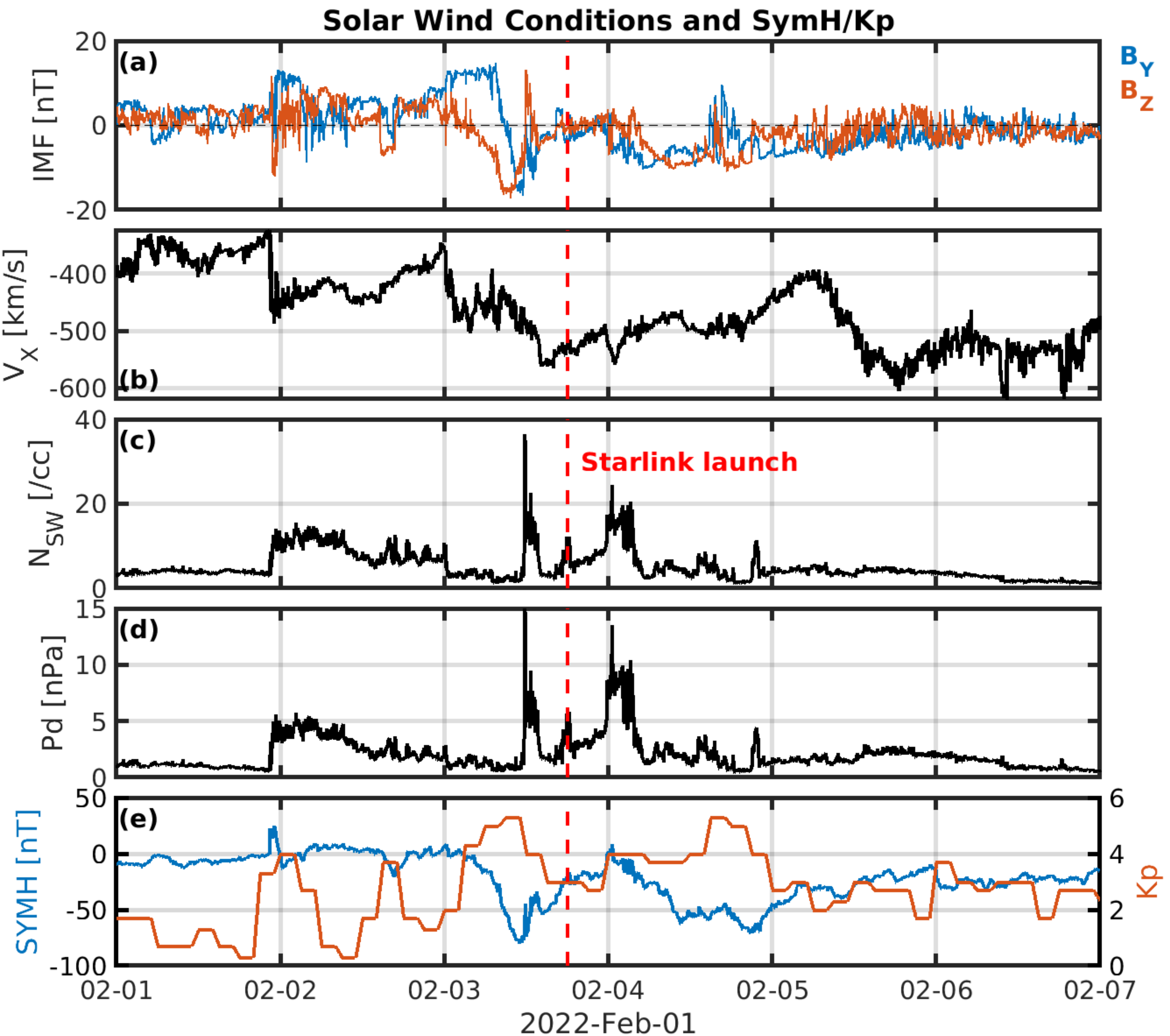

Solar Wind Conditions and SymH/Kp
(a)
IMF [nT]
B_Y
B_Z
(b)
V_X [km/s]
(c)
N_{SW} [/cc]
Starlink launch
(d)
Pd [nPa]
(e)
SYMH [nT]
Kp
02-01
02-02
02-03
02-04
02-05
02-06
02-07
2022-Feb-01

Figure2.

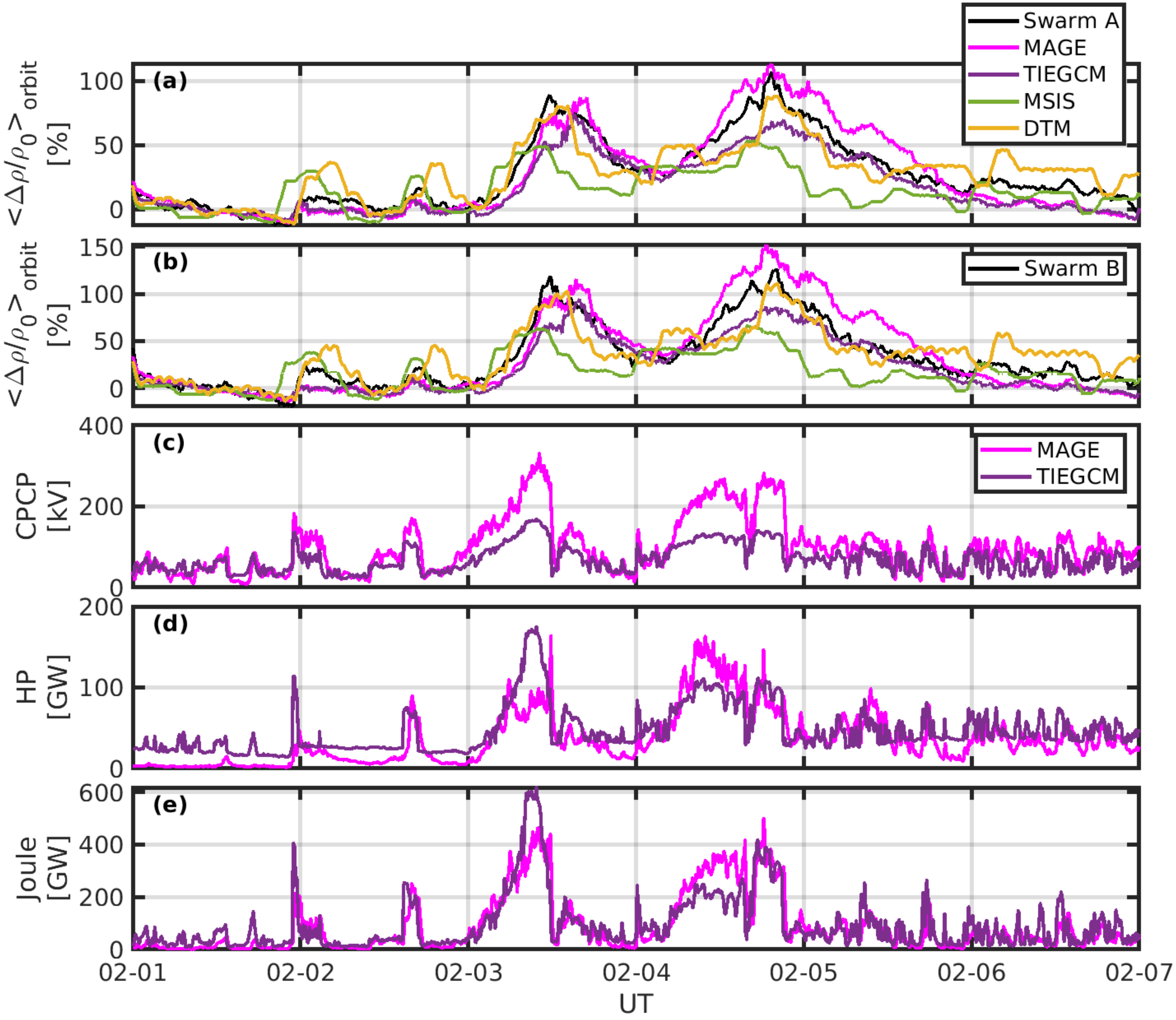

Swarm A
MAGE
TIEGCM
MSIS
DTM
(a)
$<\Delta\rho/\rho_0>_{orbit}$ [%]
100
50
0
(b)
Swarm B
150
100
50
0
(c)
MAGE
TIEGCM
CPCP [kV]
400
200
0
(d)
HP [GW]
200
100
0
(e)
Joule [GW]
600
400
200
0
02-01
02-02
02-03
02-04
02-05
02-06
02-07
UT

Figure3.

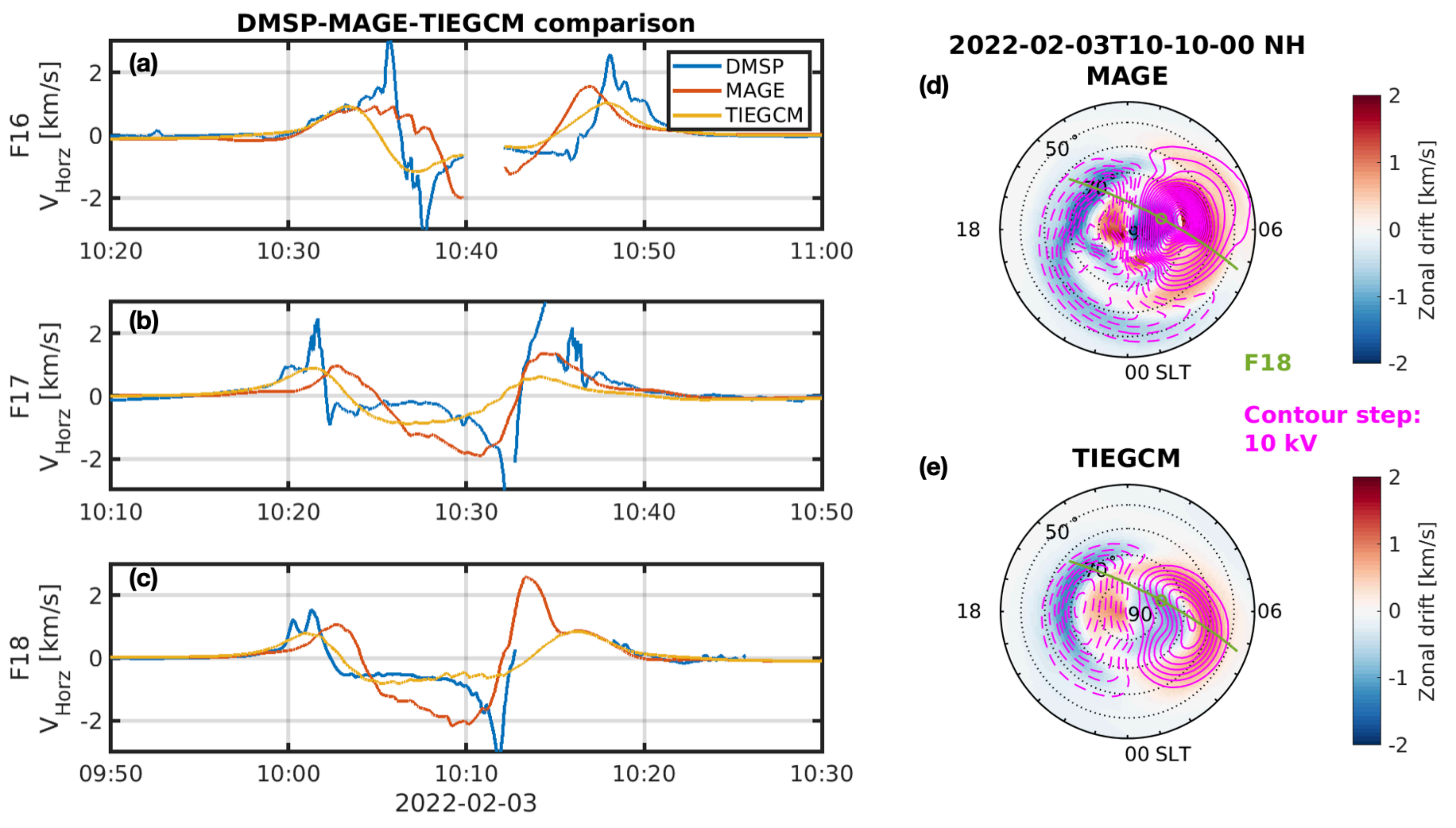

DMSP-MAGE-TIEGCM comparison
(a)
DMSP
MAGE
TIEGCM
F16 V_{Horz} [km/s]
10:20
10:30
10:40
10:50
11:00
(b)
F17 V_{Horz} [km/s]
10:10
10:20
10:30
10:40
10:50
(c)
F18 V_{Horz} [km/s]
09:50
10:00
10:10
10:20
10:30
2022-02-03
2022-02-03T10-10-00 NH
(d)
MAGE
18
06
00 SLT
F18
Zonal drift [km/s]
Contour step:
10 kV
(e)
TIEGCM

Figure4.

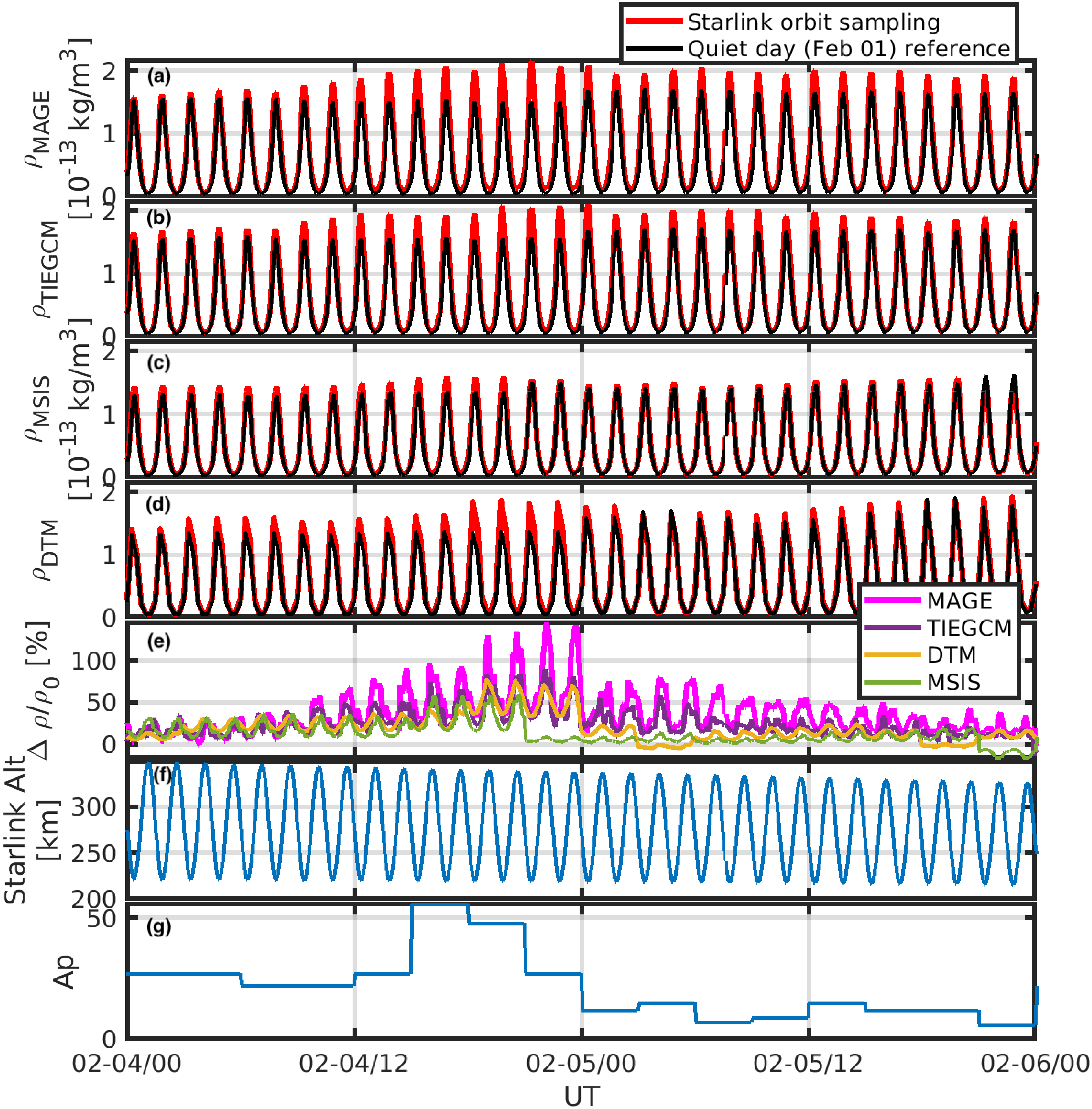

Starlink orbit sampling
Quiet day (Feb 01) reference
(a)
ρ_{MAGE} $[10^{-13}$ kg/m$^3]$
(b)
ρ_{TIEGCM}
(c)
ρ_{MSIS} $[10^{-13}$ kg/m$^3]$
(d)
ρ_{DTM}
(e)
MAGE
TIEGCM
DTM
MSIS
$\Delta\ \rho/\rho_0$ [%]
(f)
Starlink Alt [km]
(g)
Ap
02-04/00
02-04/12
02-05/00
02-05/12
02-06/00
UT

Figure5.

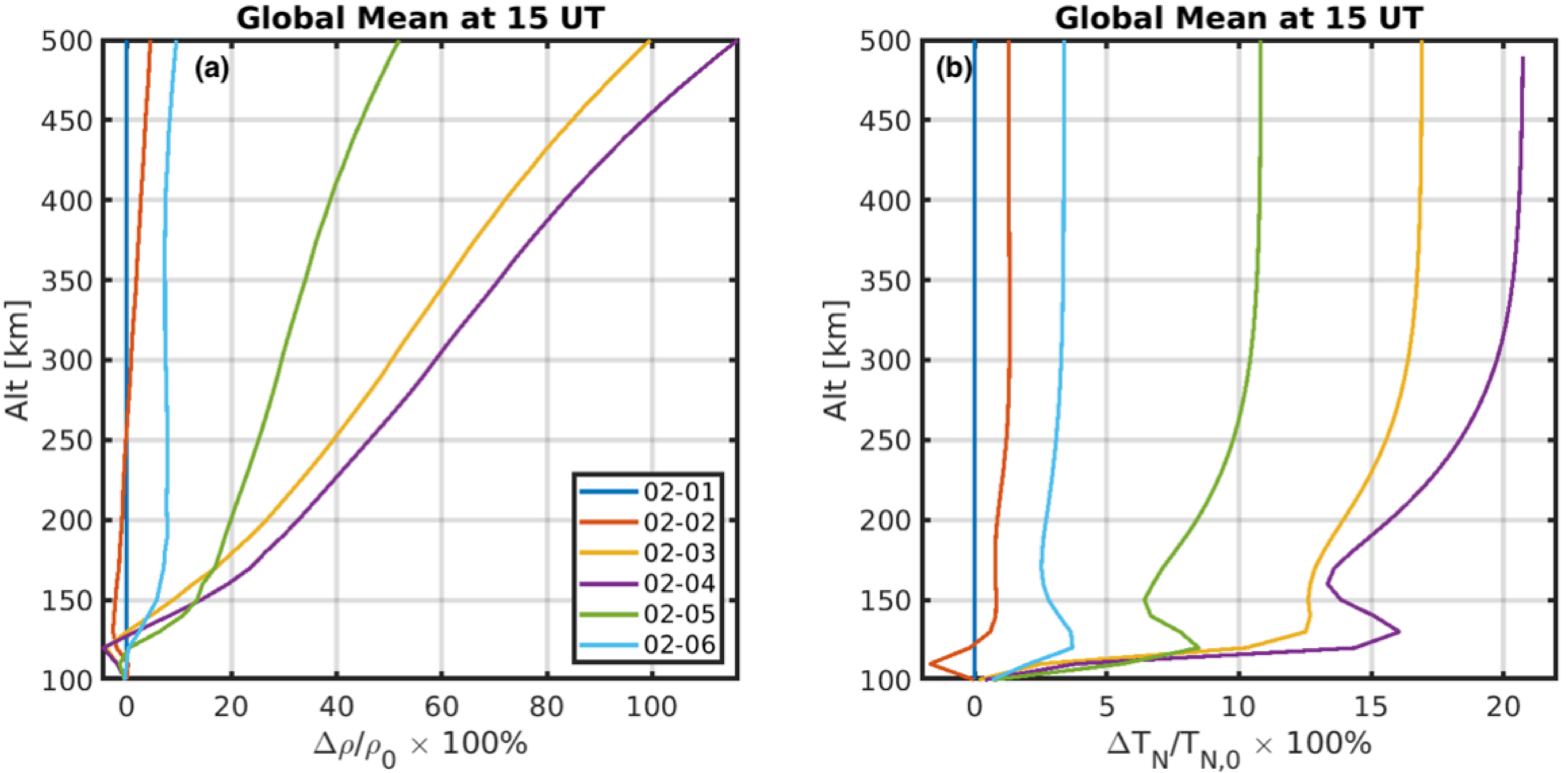

Global Mean at 15 UT
(a)
Alt [km]
$\Delta\rho/\rho_0 \times 100\%$
02-01
02-02
02-03
02-04
02-05
02-06
Global Mean at 15 UT
(b)
Alt [km]
$\Delta T_N/T_{N,0} \times 100\%$

Figure6.

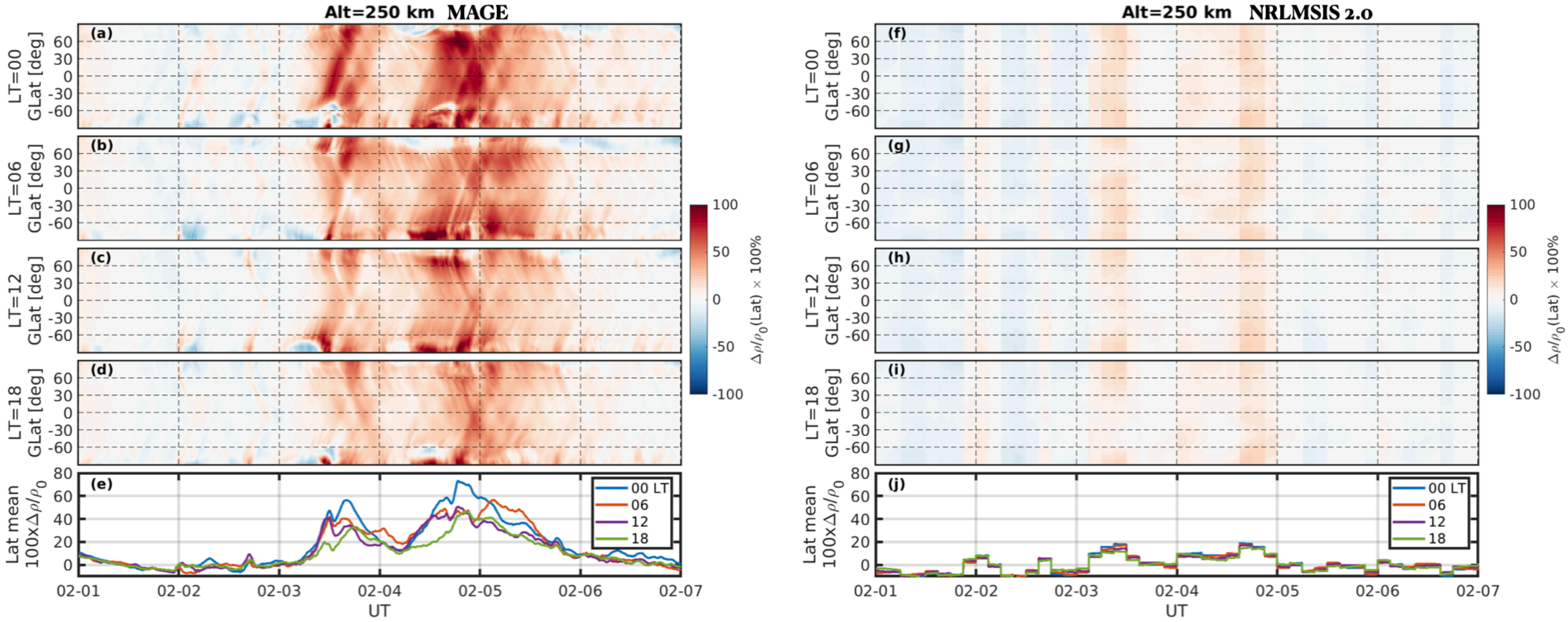

Alt=250 km MAGE
Alt=250 km NRLMSIS 2.0
(a)
(b)
(c)
(d)
(e)
(f)
(g)
(h)
(i)
(j)
LT=00 GLat [deg]
LT=06 GLat [deg]
LT=12 GLat [deg]
LT=18 GLat [deg]
Lat mean 100xΔρ/ρ0
Δρ/ρ0(Lat) × 100%
00 LT
06
12
18
02-01
02-02
02-03
02-04
02-05
02-06
02-07
UT

Figure7.

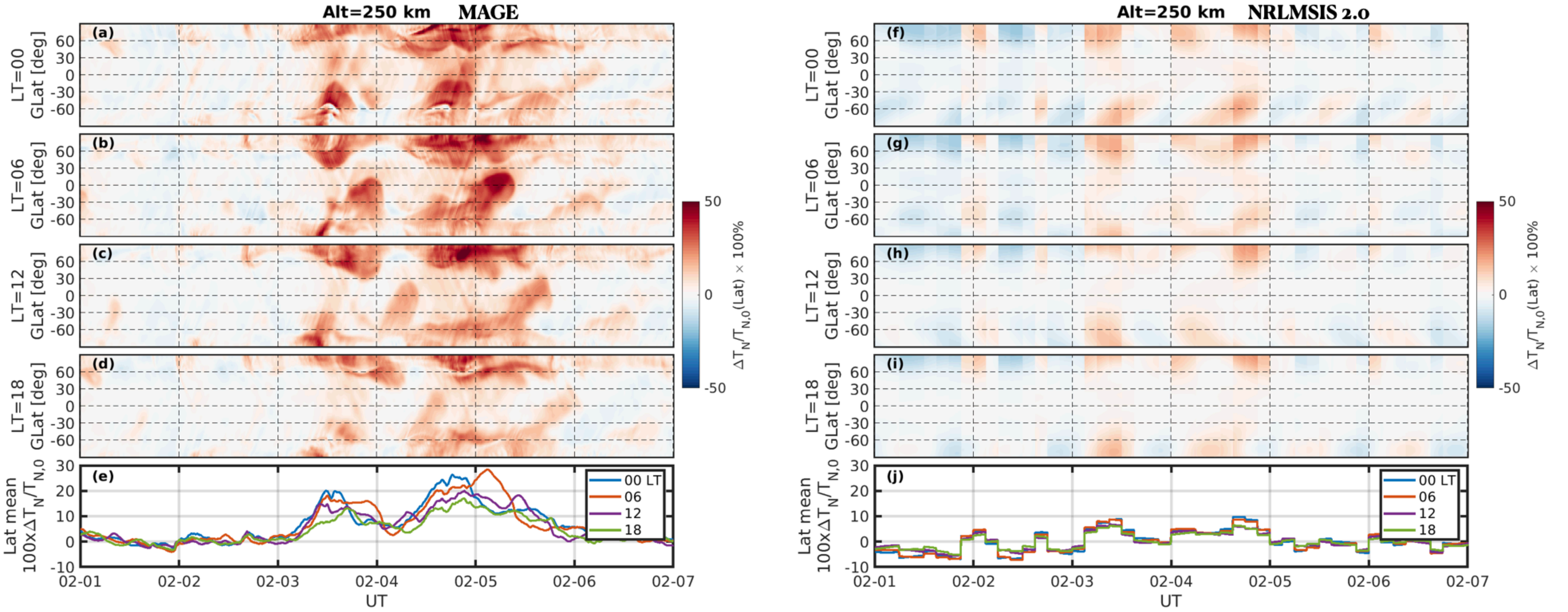
Alt=250 km MAGE
Alt=250 km NRLMSIS 2.0
(a)
(b)
(c)
(d)
(e)
(f)
(g)
(h)
(i)
(j)
LT=00 GLat [deg]
LT=06 GLat [deg]
LT=12 GLat [deg]
LT=18 GLat [deg]
Lat mean 100×ΔT_N/T_N,0
ΔT_N/T_N,0(Lat) × 100%
00 LT
06
12
18
UT
02-01
02-02
02-03
02-04
02-05
02-06
02-07